

# Tunable Chern insulator with optimally shaken lattices

Albert Verdeny and Florian Mintert

*Department of Physics, Imperial College London, London SW7 2AZ, United Kingdom*

(Received 13 April 2015; published 9 December 2015)

Driven optical lattices permit the engineering of effective dynamics with well-controllable tunneling properties. By specifically designing polychromatic driving forces, we describe how an optimal realization of a tunable Chern insulator can be achieved with a system of interacting particles on a shaken hexagonal lattice. Its implementation does not require shallow lattices and favors the study of strongly correlated phases with nontrivial topology.

DOI: [10.1103/PhysRevA.92.063615](https://doi.org/10.1103/PhysRevA.92.063615)

PACS number(s): 67.85.-d, 03.65.Vf, 03.75.Lm

## I. INTRODUCTION

The manipulation of quantum systems has reached levels of accuracy that allows controlled variation of their properties. This permits extremely precise investigations of physical processes and opens up the opportunity to design materials for scientific and economic applications. In particular, the last years have witnessed an increasing interest in topological phases of matter largely motivated by promising applications such as topological quantum computing [1] or physical phenomena such as the quantum spin Hall effect [2–4].

Systems with topological properties can be classified with topological invariants whose nonzero values indicate nontrivial phases [5]. Pioneering work in this field was done in the context of the integer quantum Hall effect, when it was shown that the quantization of the Hall conductance is directly related to the first Chern invariant [6]. Thereafter, Haldane demonstrated with a model of particles tunneling on an hexagonal lattice [7] that a net magnetic field is not necessary for the quantization of the Hall conductance, owing to the topological nature of the model. Remarkably, the Haldane model has been recently experimentally implemented [8] in a shallow shaken optical lattice taking advantage of an interplay of intrinsic and driving-induced next-nearest-neighbor tunneling processes.

Periodically driven optical lattices offer an extraordinary platform to engineer controlled dynamics. A number of theoretical [9–14] and experimental [8,15–18] works have demonstrated the possibility to modify the system dynamics in a controlled fashion and to generate diverse effects that include coherent destruction of tunneling [15,19] and the creation of synthetic magnetic fields [16–18] or topological properties [8].

Even though the effective dynamics that a driven system undergoes crucially depends on the specific time-dependent driving force, rather simple driving forces are usually employed. Nevertheless, as demonstrated in various fields, including chemistry [20,21], nuclear magnetic resonance [22,23], quantum information [24–26], and many-body systems [27], essentially any desired dynamics can be induced with the appropriate choice of polychromatic driving at desired instances of time or during an extended time window [28,29].

In this article, we show an optimal implementation of a Chern insulator in terms of a polychromatically driven, deep hexagonal lattice. We demonstrate how the parameters of the system can be tuned with suitably chosen driving forces, which

permits one to access the entire topological diagram. The possibility to realize topologically nontrivial phases in deep lattices with accurately tunable system parameters facilitates the investigation of exotic strongly correlated states by, e.g., choosing the system parameters such that the energy band becomes close to flat [30].

In Sec. II, we briefly introduce the concept of effective Hamiltonians of driven systems. In Sec. III, we derive the effective Hamiltonian of particles on a shaken hexagonal lattice and describe its topological properties. Finally, in Sec. IV, we employ pulse-shaping techniques to design polychromatic driving protocols (i.e., driving forces containing more than one frequency component) that yield an optimal and tunable realization of a Chern insulator.

## II. EFFECTIVE HAMILTONIANS

Driven systems can be used as quantum simulators due to the possibility to approximate their dynamics in terms of a time-independent effective Hamiltonian. According to the Floquet theorem [31], the time-evolution operator of a periodic Hamiltonian  $H(t) = H(t + T)$  can be written as

$$U(t) = U_F^\dagger(t) e^{-iH_{\text{eff}}t} U_F(0), \quad (1)$$

where  $U_F(t)$  is a  $T$ -periodic unitary and  $H_{\text{eff}}$  defines a time-independent effective Hamiltonian. The value of the periodic unitary at  $t = 0$  is not unambiguously defined by the driven system but it can be rather chosen for convenience by suitably transforming the effective Hamiltonian. The decomposition in Eq. (1) implies that the distance between the exact dynamics  $U(t)$  and the effective dynamics  $U_{\text{eff}}(t) = e^{-iH_{\text{eff}}t}$  induced by  $H_{\text{eff}}$  is bounded,

$$\|U(t) - U_{\text{eff}}(t)\| \leq \|1 - U_F^\dagger(t)\| + \|1 - U_F(0)\|. \quad (2)$$

Consequently, if the unitary  $U_F(t)$  is sufficiently close to the identity during an entire period, the dynamics of the system can be well approximated by the effective time-evolution operator  $U_{\text{eff}}(t)$  for all times. This is typically satisfied in a suitable fast-driving regime where the driving frequency  $\omega = 2\pi/T$  is the largest energy scale of the system. In this regime, the periodic unitary  $U_F(t)$  remains almost constant for all times [i.e.,  $U_F(t) \approx U_F(0)$ ], because it does not have time to significantly vary during the short time intervals  $T$ . If the unitary  $U_F(0)$  is chosen to be sufficiently close to the identity, then  $U_F(t) \approx 1$  and thus  $U(t) \approx U_{\text{eff}}(t)$ .

In general, the effective Hamiltonian  $H_{\text{eff}}$  is difficult to find exactly. Yet, it can be calculated in a perturbative

expansion

$$H_{\text{eff}} = H_{\text{eff}}^{(0)} + H_{\text{eff}}^{(1)} + \dots \quad (3)$$

in powers of  $\omega^{-1}$  using different methods [32–35]. The lowest-order term  $H_{\text{eff}}^{(0)} = H_0$  corresponds to the average or static Fourier component of the Hamiltonian  $H(t)$ . Higher-order terms of the effective Hamiltonian, on the other hand, explicitly depend on  $U_F(0)$ . For convenience, we use the choice of  $U_F(0)$  that leads to [36]

$$H_{\text{eff}}^{(1)} = \frac{1}{\omega} \sum_{n=1}^{\infty} \frac{1}{n} [H_n, H_{-n}], \quad (4)$$

with the Fourier components  $H_n = \frac{1}{T} \int_0^T H(t) e^{-in\omega t} dt$  of the periodic Hamiltonian  $H(t) = \sum_n H_n e^{in\omega t}$ .

### III. SHAKEN HEXAGONAL LATTICE

We start with a system of spinless bosons or fermions on a shaken hexagonal optical lattice that can be described by the time-dependent Hamiltonian

$$H(t) = H_{\text{kin}}(t) + H_{\text{int}}. \quad (5)$$

The kinetic term reads

$$H_{\text{kin}}(t) = \sum_i \mathbf{c}_{\mathbf{r}_i}^\dagger G_0(t) \mathbf{c}_{\mathbf{r}_i} + \sum_i \sum_{k=1}^2 (\mathbf{c}_{\mathbf{r}_i + \mathbf{b}_k}^\dagger G_k(t) \mathbf{c}_{\mathbf{r}_i} + \text{H.c.}) \quad (6)$$

and characterizes the driving of the system in a suitable reference frame where the time dependence of the driving is incorporated in the tunneling rates [10]. The interaction term  $H_{\text{int}}$  describes interparticle interactions of particles in a deep optical lattice potential [37] and can be expressed as

$$H_{\text{int}} = U \sum_i \mathbf{c}_{\mathbf{r}_i}^\dagger \mathbf{c}_{\mathbf{r}_i}^\dagger \mathbf{c}_{\mathbf{r}_i} \mathbf{c}_{\mathbf{r}_i}. \quad (7)$$

The summations over the index  $i$  in Eqs. (6) and (7) are performed over the positions  $\mathbf{r}_i$  of all unit cells of the hexagonal lattice, which we consider to be infinite or with periodic boundary conditions. The vectors

$$\mathbf{c}_{\mathbf{r}_i}^\dagger = (c_{A,i}^\dagger, c_{B,i}^\dagger), \quad \mathbf{c}_{\mathbf{r}_i} = (c_{A,i}, c_{B,i})^T \quad (8)$$

are given in terms of the operators  $c_{A/B,i}^{(\dagger)}$ , which create or annihilate a particle at the site  $A$  or  $B$  of the  $i$ th unit cell (depicted in Fig. 1 with red and green dots, respectively) and satisfy the usual commutation or anticommutation relations, depending on whether particles are fermions or bosons. The vectors  $\mathbf{b}_1 = a(\sqrt{3}, 0)$  and  $\mathbf{b}_2 = \frac{a}{2}(-\sqrt{3}, 3)$  are illustrated in Fig. 1 and correspond to two primitive vectors that span the underlying triangular Bravais lattice, with  $a$  denoting the distance between nearest-neighbor (NN) sites. The matrix  $G_0(t)$  in Eq. (6) describes the tunneling (or on-site energies) within the same unit cell, whereas  $G_1(t)$  and  $G_2(t)$  describe the tunneling among neighboring unit cells. In the basis defined by the vectors in Eq. (8), the time-dependent matrices in Eq. (6)

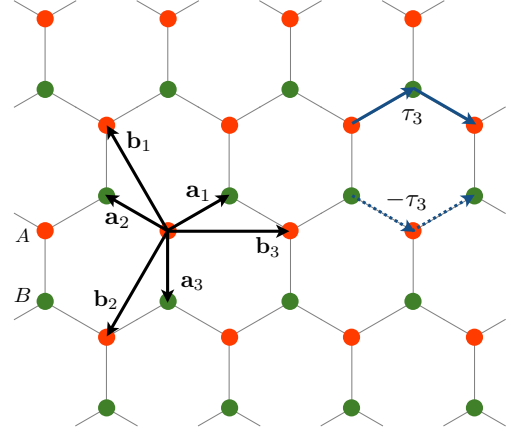


FIG. 1. (Color online) Sketch of the hexagonal lattice constructed with a triangular Bravais lattice spanned by two of the three vectors  $\mathbf{b}_1$ ,  $\mathbf{b}_2$ , and  $\mathbf{b}_3$  and a two-point basis comprising the sites  $A$  (red) and  $B$  (green). The vectors  $\mathbf{a}_1$ ,  $\mathbf{a}_2$ , and  $\mathbf{a}_3$  connect the different neighboring lattice sites. The relative sign between the rates of the effective next-nearest-neighbor tunneling along the direction  $\mathbf{b}_3$  is exemplified in blue.

read

$$G_0(t) = \begin{pmatrix} \Delta & g_{\mathbf{a}_3}^*(t) \\ g_{\mathbf{a}_3}(t) & -\Delta \end{pmatrix}, \quad (9)$$

$$G_1(t) = \begin{pmatrix} 0 & 0 \\ g_{\mathbf{a}_2}(t) & 0 \end{pmatrix}, \quad (10)$$

$$G_2(t) = \begin{pmatrix} 0 & g_{\mathbf{a}_1}^*(t) \\ 0 & 0 \end{pmatrix}. \quad (11)$$

The quantities  $\pm\Delta$  define an on-site energy of the sites such that there is an overall energy difference  $2\Delta$  between the on-site energy of the lattice sites  $A$  and  $B$ . The time-dependent NN rates read

$$g_{\mathbf{a}_k}(t) = j_0 e^{i\chi_{\mathbf{a}_k}(t)} \quad (12)$$

and characterize the rate for a particle at a site  $\mathbf{r}_i$  to tunnel to  $\mathbf{r}_i + \mathbf{a}_k$ , where the vectors  $\mathbf{a}_k$  are defined to connect neighboring sites, as depicted in Fig. 1. They read  $\mathbf{a}_1 = \frac{a}{2}(\sqrt{3}, 1)$ ,  $\mathbf{a}_2 = \frac{a}{2}(-\sqrt{3}, 1)$ , and  $\mathbf{a}_3 = -\mathbf{a}_1 - \mathbf{a}_2$ . The time-dependent tunneling rates in Eq. (12) are thus characterized by the real NN tunneling rate  $j_0$  of the undriven system and the periodic function

$$\chi_{\mathbf{a}_k}(t) = \int_0^t d\tau \mathbf{F}(\tau) \cdot \mathbf{a}_k - \frac{1}{T} \int_0^T dt \int_0^t d\tau \mathbf{F}(\tau) \cdot \mathbf{a}_k, \quad (13)$$

defined in terms of the external driving force  $\mathbf{F}(t)$  that produces the shaking, and the direction of tunneling  $\mathbf{a}_k$ .

As theoretically expected and experimentally confirmed [8], the dynamics of the system in a fast driving regime can be captured very well by the truncated effective Hamiltonian

$$H_{\text{dh}} = H_{\text{eff}}^{(0)} + H_{\text{eff}}^{(1)}. \quad (14)$$

Since the leading-order effective Hamiltonian  $H_{\text{eff}}^{(0)}$  is given by the temporal average of  $H(t)$  in Eq. (5), it contains the

same physical processes as the undriven system. The on-site energies  $\pm\Delta$  and the interactions  $H_{\text{int}}$  remain unchanged, but the effective NN tunneling rates become the directionality-dependent quantities  $g_{\mathbf{a}_k}^0 = \frac{1}{T} \int_0^T dt g_{\mathbf{a}_k}(t)$ . On the contrary, the first-order term  $H_{\text{eff}}^{(1)}$  contains new tunneling processes and reads

$$H_{\text{eff}}^{(1)} = \sum_i \mathbf{c}_{\mathbf{r}_i}^\dagger B_0 \mathbf{c}_{\mathbf{r}_i} + \sum_i \sum_{k=1}^3 (\mathbf{c}_{\mathbf{r}_i+\mathbf{b}_k}^\dagger B_k \mathbf{c}_{\mathbf{r}_i} + \text{H.c.}), \quad (15)$$

where  $\mathbf{b}_3 = -(\mathbf{b}_1 + \mathbf{b}_2)$  and the effective tunneling matrices

$$B_k = \begin{pmatrix} \tau_k & 0 \\ 0 & -\tau_k \end{pmatrix}, \quad (16)$$

$k = 0, 1, 2, 3$ , are given in terms of the on-site energy  $\tau_0 = \sum_{i=1}^3 \beta(\mathbf{a}_i, -\mathbf{a}_i)$  and the tunneling rates

$$\tau_1 = \beta(\mathbf{a}_2, -\mathbf{a}_3), \quad (17)$$

$$\tau_2 = \beta(\mathbf{a}_3, -\mathbf{a}_1), \quad (18)$$

$$\tau_3 = \beta(\mathbf{a}_1, -\mathbf{a}_2). \quad (19)$$

The quantity

$$\beta(\mathbf{a}_i, \mathbf{a}_j) = \sum_{n=1}^{\infty} \frac{1}{n\omega} (g_{\mathbf{a}_i}^{-n} g_{\mathbf{a}_j}^n - g_{\mathbf{a}_j}^{-n} g_{\mathbf{a}_i}^n) \quad (20)$$

that defines the effective rates is expressed in terms of the Fourier components  $g_{\mathbf{a}_j}^n = \frac{1}{T} \int_0^T g_{\mathbf{a}_j}(t) e^{-in\omega}$  of the time-dependent tunneling rates in Eq. (12). The rates  $\tau_k$  with  $k = 1, 2, 3$  describe emergent next-nearest-neighbor (NNN) tunneling processes that result from a virtual tunneling process over a neighboring site. The relative sign in  $B_k$  between the different rates  $\tau_k$  and  $-\tau_k$ , exemplified in Fig. 1, is a fundamental symmetry that is independent of the specific driving force  $\mathbf{F}(t)$  [38]. Due to this symmetry, the emergent NNN tunneling rates discussed above are, in general, not equivalent to those of the paradigmatic Haldane model [7], where the two tunneling rates are complex conjugated with respect to each other. Only for purely imaginary rates  $\tau_k^* = -\tau_k$ ,  $k = 1, 2, 3$ , do the NNN tunneling rates of the two models coincide. Consequently, it is fundamentally impossible to implement the full topological diagram of the Haldane model with the present lattice shaking approach without nonvanishing real NNN tunneling rates in the undriven system.

### Topological band structure

Despite the differences between the Haldane model Hamiltonian and the effective Hamiltonian in Eq. (14), the two models share similar topological properties. As we shall later demonstrate, it is possible to find a driving force  $\mathbf{F}(t)$  yielding isotropic tunneling rates, namely,  $g_{\mathbf{a}_k}^0 = j_1$  and  $\tau_k = j_2 e^{i\phi}$  for all directions  $k = 1, 2, 3$ , where  $j_1$  and  $j_2$  are positive real numbers and  $\phi$  is defined in the interval  $(-\pi, \pi]$ . The noninteracting part of the effective Hamiltonian can then be written in quasimomentum space as  $H_{\text{dh}} - H_{\text{int}} = \sum_{\mathbf{k}} \mathbf{c}_{\mathbf{k}}^\dagger H(\mathbf{k}) \mathbf{c}_{\mathbf{k}}$ , where  $\mathbf{c}_{\mathbf{k}}$  are the vector momentum creation

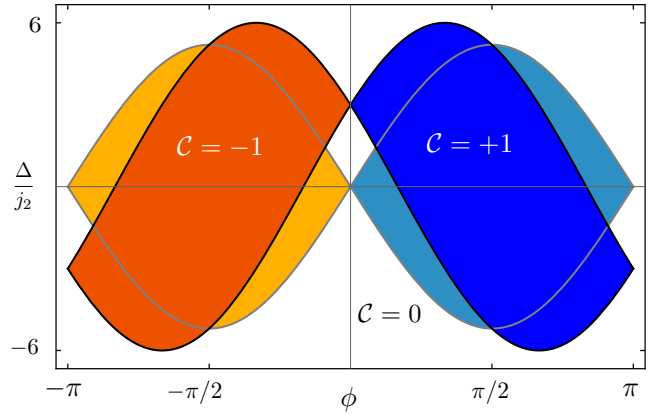


FIG. 2. (Color online) Phase diagram of the isotropic effective Hamiltonian in Eq. (21) (black lines and dark colors) overlapped with the phase diagram of the Haldane model [39] (gray lines and lighter colors), giving the Chern number  $\mathcal{C}$  of the lowest-energy band as a function of the phase  $\phi$  and ratio  $\Delta/j_2$ . Orange represents  $\mathcal{C} = -1$ , blue  $\mathcal{C} = 1$ , and white  $\mathcal{C} = 0$ . For  $\phi = \pm\pi/2$  the Chern number of the two Hamiltonians coincide independently of  $\Delta/j_2$ .

and annihilation operators and

$$H(\mathbf{k}) = \sum_{i=1}^3 h_i(\mathbf{k}) \sigma_i \quad (21)$$

is defined in terms of the Pauli matrices  $\sigma_i$  and

$$h_1(\mathbf{k}) = j_1 [1 + \cos(\mathbf{k} \cdot \mathbf{b}_1) + \cos(\mathbf{k} \cdot \mathbf{b}_2)], \quad (22)$$

$$h_2(\mathbf{k}) = j_1 [\sin(\mathbf{k} \cdot \mathbf{b}_1) - \sin(\mathbf{k} \cdot \mathbf{b}_2)], \quad (23)$$

$$h_3(\mathbf{k}) = \Delta + 2j_2 \sum_{i=1}^3 \cos(\mathbf{k} \cdot \mathbf{b}_i + \phi). \quad (24)$$

The topological diagram of this model, displaying the Chern number [5] as a function of the Hamiltonian parameters  $\Delta/j_2$  and  $\phi$ , can be readily calculated [40] and it is shown in Fig. 2. The transition between different topological phases—indicated with a solid black line—corresponds to parameters of the Hamiltonian for which the gap between the two energy bands  $\epsilon_{\pm}(\mathbf{k}) = \sqrt{h_1^2(\mathbf{k}) + h_2^2(\mathbf{k}) + h_3^2(\mathbf{k})}$  closes. For comparison, we also display the analogous topological diagram of the isotropic Haldane model Hamiltonian [39]. Only for  $\phi = \pm\pi/2$  do the two Hamiltonians coincide, consistently with the diagram in Fig. 2.

### IV. OPTIMAL DESIGN OF DRIVING

In order to assess to what extent the entire parameter regime of the topological diagram in Fig. 2 can be realistically explored, it is necessary to correctly identify driving forces  $\mathbf{F}(t)$  that lead to isotropic effective tunneling rates with controllable amplitudes and phase  $\phi$ . Since the topological band structure emerges as a consequence of the interplay between the NN and NNN tunneling processes, it is important that the relative effect of the NNN tunneling with respect to NN tunneling, given by the ratio  $j_2/j_1$ , is sufficiently large. Nevertheless, these two tunneling processes are of different orders of magnitude,

since  $j_1 \propto j_0$  and  $j_2 \propto j_0^2/\omega$ . As the ratio  $j_2/j_1$  is proportional to  $j_0/\omega$ , it could easily be increased through a decrease of the driving frequency  $\omega$ . This, however, could compromise the validity of the high-frequency expansion of the effective Hamiltonian. For this reason, we consider a small fixed ratio  $j_0/\omega$  to be determined according to the experimental setup and aim at finding a driving force with a set of parameters  $\mathbf{p}$  that maximize the proportionality factor  $\frac{j_2}{j_1} \frac{\omega}{j_0}$  between  $j_2/j_1$  and  $j_0/\omega$ . Since the amplitude  $j_2$  is directly related to  $\phi$ , we introduce  $\phi = \phi_{\text{tg}}$  as a constraint for the maximization, where  $\phi_{\text{tg}}$  is the desired phase that we target. Additionally,  $j_1$  should be sufficiently large with respect to the bare tunneling rate  $j_0$  in order to avoid that the effective tunneling processes appear at the expense of slowing down the dynamics as compared to the undriven system. We therefore introduce the additional constraint  $j_1/j_0 \geq r_{\text{th}}$ , where the threshold value  $r_{\text{th}}$  can be chosen from the interval  $0 \leq r_{\text{th}} \leq 1$ . We thus aim at finding a driving force targeting: (i) isotropy  $g_{\mathbf{a}_k}^0 = j_1$  and  $\tau_k = j_2 e^{i\phi}$ ,  $k = 1, 2, 3$ ; (ii) controllability of the phase  $\phi$ ; and (iii) enhancement of the NNN tunneling rates through the maximization

$$R(\phi_{\text{tg}}, r_{\text{th}}) = \left\{ \max_{\mathbf{p}} \frac{j_2}{j_1} \frac{\omega}{j_0} \mid \frac{j_1}{j_0} \geq r_{\text{th}}; \phi = \phi_{\text{tg}} \right\}, \quad (25)$$

performed over a set of free driving parameters  $\mathbf{p}$ .

For a monochromatic driving force [8,41–43], the effective NNN tunneling rates  $\tau_k$  become purely imaginary and, thus, only the points  $\phi = \pm\pi/2$  in Fig. 2 can be accessed. However, this strong limitation can be overcome by specifically designing the driving pulse to satisfy our requirements.

Despite the highly nonlinear dependence that the effective tunneling rates have on the driving force, we find analytic expressions for  $g_{\mathbf{a}_k}^0$  and  $\tau_k$  in terms of driving parameters by using multidimensional Bessel functions, which we introduce in Appendix A. This allows us to identify the structure of two driving forces  $\mathbf{F}_+(t)$  and  $\mathbf{F}_-(t)$  that lead to isotropic tunneling rates independently of their free parameters, as derived in Appendix B. Consequently, requirement (i) above is automatically satisfied [44], which allows the examination of the subsequent target properties. The general form of the driving forces  $\mathbf{F}_{\pm}(t)$  containing  $N$  different frequency harmonics reads

$$\mathbf{F}_{\pm}(t) = \sum_{n=1}^N A_n [\cos(\omega_n t - \delta_n) \mathbf{e}_1 + \cos(\omega_n t - \delta_n^{\pm}) \mathbf{e}_2], \quad (26)$$

with the two perpendicular vectors  $\mathbf{e}_1 = (\mathbf{a}_1 - \mathbf{a}_2)/\sqrt{3}$  and  $\mathbf{e}_2 = -\mathbf{a}_3$ , the phases

$$\delta_n^{\pm} = \delta_n \pm (-1)^n \pi/2, \quad (27)$$

and the frequencies

$$\omega_m = \frac{1}{4}[6m - (-1)^m - 3]\omega, \quad (28)$$

which parametrize all positive integer multiples of  $\omega$  except those that are multiples of  $3\omega$ . The fact that no multiples of  $3\omega$  are present in the driving force is a consequence of the  $2\pi/3$  rotational symmetry of the lattice, as described at the end of Appendix B. Because the overall phase of the driving force is irrelevant in the fast-driving regime, we choose  $\delta_1 = 0$  in the following. The remaining  $2N - 1$  driving parameters ( $N$

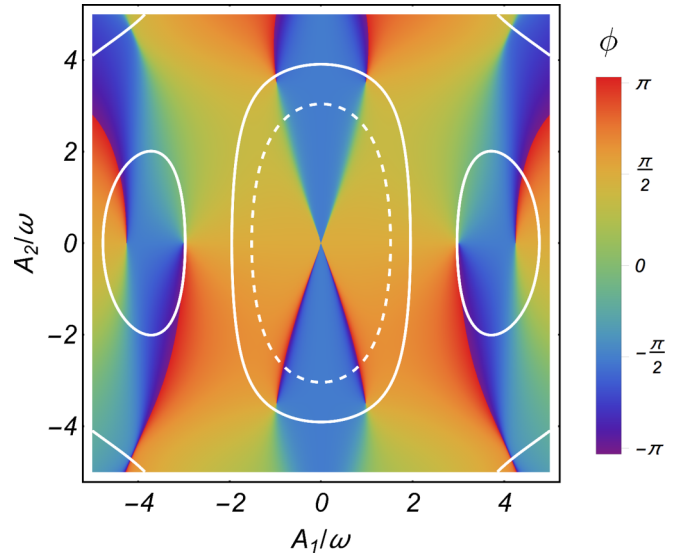


FIG. 3. (Color online) Phase  $\phi$  of the complex effective next-nearest-neighbor tunneling rates as a function of  $A_1/\omega$  and  $A_2/\omega$  for a force  $\mathbf{F}_+(t)$  with  $N = 2$  and  $\delta_2 = \pi/2$ . All phases can be explored with a suitable choice of  $A_1$  and  $A_2$ . The dashed and solid white lines indicate the contour lines for  $j_1/j_0 = 0.5$  and  $j_1/j_0 = 0.25$  and limit the region of accessible phases given a constraint with  $r_{\text{th}} = 0.5$  or  $r_{\text{th}} = 0.25$ , respectively.

amplitudes and  $N - 1$  phases) comprise the set  $\mathbf{p}$  and need to be chosen so that the requirements (ii) and (iii) are satisfied.

### A. Bichromatic driving force

In order to ease an experimental implementation, we consider the simplest polychromatic force with two frequency harmonics (i.e.,  $N = 2$ ), which contains three driving parameters: two amplitudes  $A_1$  and  $A_2$ , and a relative phase  $\delta_2$ . We analytically find that, if  $\delta_2 = 0, \pm\pi$ , the real part of  $\tau_k$  again vanishes, similarly to the monochromatic case. However, for  $\delta_2 \neq 0, \pm\pi$  and an appropriate choice of driving amplitudes, the entire range of phases  $\phi \in (-\pi, \pi]$  can be realized, satisfying thus requirement (ii), as illustrated in Fig. 3. Consequently, in a deep optical lattice implementation of the system where interactions are present, only the use of, at least, bichromatic driving permits one to achieve any desired phase  $\phi$  of the effective NNN tunneling rates. The possibility to tune the effective Hamiltonian parameters and scan the different regions of the topological diagram is especially relevant for the interacting system of particles we consider, since the emergence of strongly correlated many-body ground states importantly depends on the details of the system's implementation [30,45,46].

The maximization described in point (iii) leads to a significant effective NNN tunneling rate for any desired phase, which strongly suggests that NNN tunneling rates with an arbitrary phase could be experimentally detected. Yet, considerably different results are obtained depending on the phase  $\phi_{\text{tg}}$  and threshold rate  $r_{\text{th}}$  that we target. In order to discuss this behavior, we plot in Fig. 4 the real and imaginary part of  $R(\phi_{\text{tg}}, r_{\text{th}}) e^{i\phi_{\text{tg}}}$  for two different values of  $r_{\text{th}}$  and for a discrete set of angles  $\phi_{\text{tg}} \in (-\pi, \pi]$ . Each data point is obtained

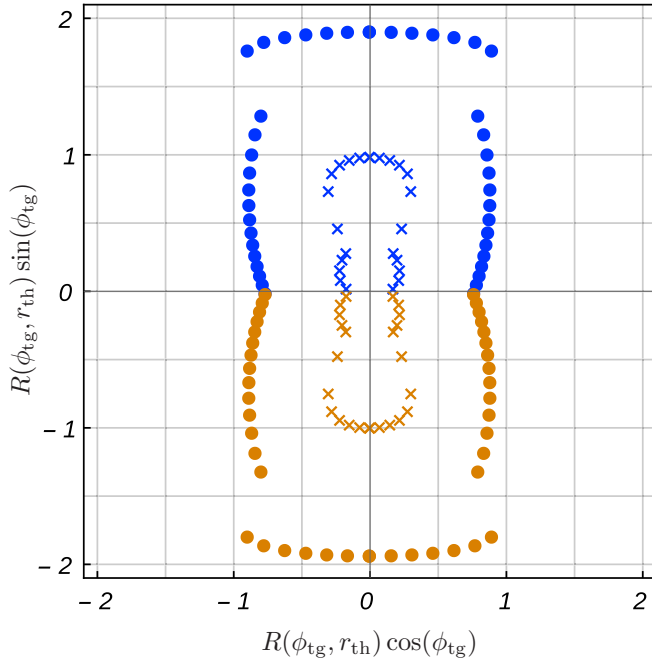


FIG. 4. (Color online) Plot of the real and imaginary part of  $R(\phi_{\text{tg}}, r_{\text{th}})e^{i\phi_{\text{tg}}}$  calculated numerically as a function of a discrete set of target phases  $\phi_{\text{tg}}$  and for two different values of  $r_{\text{th}}$ . In polar coordinates, the radius and argument of each data point coincide with  $R(\phi_{\text{tg}}, r_{\text{th}})$  and  $\phi_{\text{tg}}$ , respectively. Dots correspond to  $r_{\text{th}} = 0.25$ , and crosses to  $r_{\text{th}} = 0.5$ . The results in blue have been obtained with a driving force  $\mathbf{F}_+(t)$  and the results in orange with  $\mathbf{F}_-(t)$ .

with a numerical constrained optimization over the set of free parameters  $\mathbf{p} = (A_1/\omega, A_2/\omega, \delta_2)$ . Overall, we observe two main features.

First, for a given threshold value  $r_{\text{th}}$ , the largest values of  $R(\phi_{\text{tg}}, r_{\text{th}})$  are obtained for a range of phases close to  $\pm\pi/2$ . The lowest values correspond to phases 0 and  $\pm\pi$ , for which the effective Hamiltonian  $H_{\text{dh}}$  is time-reversal invariant. This indicates that experimentally it is easier to access the areas of the topological diagram in Eq. (2) that are near  $\phi = \pm\pi/2$ . Noteworthy, we find that for  $\phi_{\text{tg}} = \pm\pi/2$  the optimal solution of the two-frequency pulse reduces to a monochromatic force, i.e.,  $A_2 = 0$ , independently of  $r_{\text{th}}$ . Nonetheless, the maximum of  $R(\phi_{\text{tg}}, r_{\text{th}})$  does not always correspond to  $\phi_{\text{tg}} = \pm\pi/2$  for a fixed  $r_{\text{th}}$ , as can be seen in the results for  $r_{\text{th}} = 0.25$  in Fig. 4.

Second, the lower the threshold value  $r_{\text{th}}$  is for a fixed target phase  $\phi_{\text{tg}}$ , the larger  $R(\phi_{\text{tg}}, r_{\text{th}})$  can be, as a larger region in the parameter space, given by the driving parameters, can be accessed (see the contour lines in Fig. 3). Thus, there is a trade-off between the lower values of the threshold  $r_{\text{th}}$  for the ratio  $j_1/j_0$  and a higher relative enhancement  $\frac{j_2}{j_1} \frac{\omega}{j_0}$  of NNN tunneling. It is thus advisable to choose a small value of  $r_{\text{th}}$ , provided that it is sufficiently large so that tunneling is dominant in the dynamics of the system and processes such as interaction or heating can be neglected on the time scale on which tunneling occurs.

As a result of the maximization in Eq. (25), the optimal driving parameters that yield the maximum enhancement of the NNN tunneling are also obtained. We find that the optimal driving amplitudes strongly depend on the target

parameters  $\phi_{\text{tg}}$  and  $r_{\text{th}}$ . For instance, it can be observed in Fig. 3 that different values of the constraint  $r_{\text{th}}$  restrict the driving amplitudes to distinct regions, which has a clear effect on the values of the optimal driving amplitudes. In particular, optimal driving amplitudes with the constraint  $r_{\text{th}} = 0.5$  are equal to or smaller than those with the constraint  $r_{\text{th}} = 0.25$ . For all the results shown in Fig. 4, we find that the corresponding driving amplitudes are of a similar order of magnitude as the driving frequency, specifically,  $|A_2| < |A_1|$  and  $|A_1/\omega| < 3.5$ . Additionally, we observe a discontinuous behavior of the optimal driving parameters as a function of  $\phi_{\text{tg}}$ , which leads to a discontinuity in  $R(\phi_{\text{tg}}, r_{\text{th}})$ , as manifested with the  $r_{\text{th}} = 0.25$  results in Fig. 4. This can be understood in terms of the constraint  $j_1/j_0 > r_{\text{th}}$ , which restricts the parameter space to disjoint regions, as can be seen in the contour line  $j_1/j_0 = 0.25$  in Fig. 3. Depending on the targeted phase, the driving parameters might change from one region to another, yielding a discontinuity in the driving parameters and in the corresponding value of  $R(\phi_{\text{tg}}, r_{\text{th}})$ .

## B. Trichromatic driving force

When increasing the number of frequency harmonics of the force  $\mathbf{F}_{\pm}(t)$ , more driving parameters become accessible. These additional degrees of freedom can be exploited, e.g., to further increase the maximum value of  $R(\phi_{\text{tg}}, r_{\text{th}})$  targeting specific phases. A three-frequency driving force contains the set of driving parameters  $\mathbf{p} = (A_1/\omega, A_2/\omega, A_3/\omega, \delta_2, \delta_3)$ , where  $A_3$  and  $\delta_3$  correspond to the amplitude and phase associated with the frequency component  $\omega_3 = 4\omega$  in Eq. (28). Analogously to the two-frequency results, we obtain the optimal choice of  $\mathbf{p}$  with the constrained maximization in Eq. (25), with the target functional and constraints expressed analytically in terms of three-dimensional Bessel functions.

In Fig. 5, we display optimal results obtained and compare them with the  $N = 2$  results. We observe that, for the entire range of target phases  $\phi_{\text{tg}}$  except for  $\phi_{\text{tg}} = \pm\pi/2$ , optimally

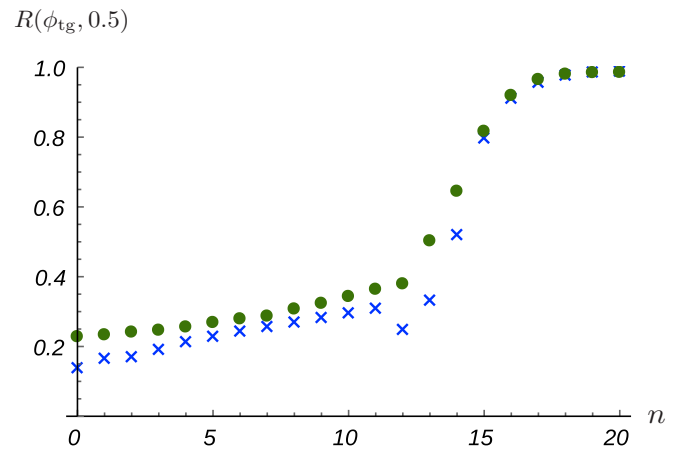


FIG. 5. (Color online) Plot of  $R(\phi_{\text{tg}}, r_{\text{th}} = 0.5)$  calculated numerically as a function of a discrete set of target phases  $\phi_{\text{tg}} = \phi_n = n\pi/40$  indexed by  $n = 0, 1, \dots, 20$ . Thus, the labels  $n = 0$  and  $n = 20$  refer to  $\phi_{\text{tg}} = 0$  and  $\phi_{\text{tg}} = \pi/2$ , respectively. The results in green correspond to a driving force  $\mathbf{F}_+(t)$  with  $N = 3$ , while in blue crosses we display for comparison the results for  $N = 2$ .

chosen forces with  $N = 3$  lead to larger values of  $R(\phi_{\text{tg}}, r_{\text{th}})$  than for bichromatic driving. Moreover, the maximum relative enhancement of the tunneling appears for small values of  $\phi_{\text{tg}}$ , which is precisely where the enhancement is most desired. Similarly to the  $N = 2$  case, we find that the optimal driving force targeting  $\phi_{\text{tg}} = \pm\pi/2$  corresponds to the monochromatic force, i.e.,  $A_2 = A_3 = 0$ .

Remarkably, the enhancement of the effective NNN tunneling (of order  $\sim\omega^{-1}$ ) as compared to the NN tunneling (of order  $\sim 1$ ) relies on the use of a higher-frequency component. This strongly suggests that the use of driving forces  $\mathbf{F}_{\pm}(t)$  with even higher-frequency harmonics, that is, with  $N > 3$ , and optimally chosen driving parameters could still further improve on the value of  $R(\phi_{\text{tg}}, r_{\text{th}})$ . Nonetheless, our results show that already a very low number of frequency components is sufficient to significantly outperform the monochromatic driving and yield significant NNN tunneling rates for any phase  $\phi$ .

## V. CONCLUSIONS

The results we have presented show that even a very low number of frequency components is sufficient to completely outperform the monochromatic driving and yield significant NNN tunneling rates with any desired phase  $\phi$ . This exemplifies the fact that the usually considered monochromatic driving can strongly limit the accessible effective dynamics and that only suitably chosen driving protocols enable the exploration of the entire accessible dynamics of the system.

Typically, polychromatic driving would induce more heating than a monochromatic realization, because a growing number of frequencies makes it harder to ensure that no undesired transitions to higher-energy bands are driven non-negligibly [47]. However, since the present prescription is based on driving patterns with very few frequencies, there is substantial freedom to identify suitable parameters that suppress such transitions. Indeed, a driving profile  $\mathbf{F}_{\text{sc}}(t)$  composed of a sine and constant intervals has been successfully realized in experiments [48] and has led to the observation of coherent dynamics over a substantial number of periods of time. The profile  $\mathbf{F}_{\text{sc}}(t)$  contains, in addition to the two leading amplitudes corresponding to the first two frequency harmonics, a tail of finite amplitudes associated with higher frequencies. Since this tail is missing for the present driving force, it is thus expected that the presently described driving protocol induces rather less heating than driving schemes whose experimental viability has been verified.

The realization of the model we describe does not require NNN tunneling in the underlying undriven system, which is a necessary requirement for the implementation of the system with deep optical lattices, where NNN tunneling is negligible and interactions are not. Moreover, the possibility to tune the parameters of the effective Hamiltonian and access its entire topological diagram is especially relevant for the study of strongly correlated many-body phases, since the specific details of the band structure are crucial in order to determine the many-body ground state [30,45,46]. We believe, thus, that the possibility to experimentally implement the effective Hamiltonian introduced in Eq. (14) naturally warrants further investigations on, e.g., the emergence of fractional quantum Hall states in this system.

Moreover, the optimal control methods used in this work can also be applied to a broad range of driven lattice systems, including, e.g., a system of spinful particles driven with a time-dependent magnetic gradient [49]. The use of optimal control techniques for driving-induced effective dynamics has thus the potential of advancing the field of quantum simulations by enabling a reliable implementation of different physical models.

## ACKNOWLEDGMENTS

We are indebted to Julian Struck, Juliette Simonet, Gregor Jotzu, Andreas Mielke, and Elizabeth von Hauff for stimulating discussions or feedback on the manuscript. Financial support by the European Research Council within the project ODYCCQUENT is gratefully acknowledged.

## APPENDIX A: MULTIDIMENSIONAL BESSEL FUNCTIONS

The effective tunneling rates of the Hamiltonian  $H_{\text{dh}}$  in Eq. (14) are given in terms of the Fourier components  $g_{\mathbf{a}_i}^n$  of the time-dependent tunneling rates; they are defined through the relation

$$g_{\mathbf{a}_k}(t) = j_0 e^{i\chi_{\mathbf{a}_k}(t)} = \sum_{n=-\infty}^{\infty} g_{\mathbf{a}_i}^n e^{in\omega t}, \quad (\text{A1})$$

with the  $T$ -periodic function  $\chi_{\mathbf{a}_k}(t)$  in Eq. (13). Motivated by the need for analytical expressions to target the properties described in points (i)–(iii) in Sec. IV, we introduce multidimensional Bessel functions as a generalization of ordinary and two-dimensional Bessel functions [50].

Ordinary  $n$ th order Bessel functions  $\mathcal{J}_n(a)$  can be defined as Fourier components of the generating function

$$e^{ia \sin(b)} = \sum_{n=-\infty}^{\infty} \mathcal{J}_n(a) e^{inb}. \quad (\text{A2})$$

Here, we generalize the Bessel functions introduced above and consider  $N$ -dimensional Bessel functions  $\mathcal{J}_n^{\mathbf{z}}(\mathbf{c}; \mathbf{d})$  defined by the generating function

$$e^{i \sum_{k=1}^N c_k \sin(z_k \tau - d_k)} = \sum_{n=-\infty}^{\infty} \mathcal{J}_n^{\mathbf{z}}(\mathbf{c}; \mathbf{d}) e^{in\tau}, \quad (\text{A3})$$

with the real vectors  $\mathbf{c} = (c_1, \dots, c_N)$  and  $\mathbf{d} = (d_1, \dots, d_N)$ , and the integer vector  $\mathbf{z} = (z_1, \dots, z_N)$ . The Fourier transform of Eq. (A3) leads to the integral representation

$$\mathcal{J}_n^{\mathbf{z}}(\mathbf{c}; \mathbf{d}) = \frac{1}{2\pi} \int_0^{2\pi} d\tau e^{i \sum_{k=1}^N c_k \sin(z_k \tau - d_k) - in\tau}. \quad (\text{A4})$$

Inserting Eq. (A2) into Eq. (A4) permits one to expand  $N$ -dimensional Bessel functions in terms of ordinary one-dimensional Bessel functions,

$$\begin{aligned} \mathcal{J}_n^{\mathbf{z}}(\mathbf{c}; \mathbf{d}) &= \sum_{\mathbf{x}} \mathcal{J}_{x_1}(c_1) \cdots \mathcal{J}_{x_N}(c_N) e^{-i\mathbf{d}\cdot\mathbf{x}} \\ &\times \frac{1}{2\pi} \int_0^{2\pi} d\tau e^{i\tau(\mathbf{z}\cdot\mathbf{x} - n)} \end{aligned} \quad (\text{A5})$$

$$= \sum_{\mathbf{x}} \mathcal{J}_{x_1}(c_1) \cdots \mathcal{J}_{x_N}(c_N) e^{-i\mathbf{d}\cdot\mathbf{x}} \delta_{\mathbf{z}\cdot\mathbf{x},n} \quad (\text{A6})$$

$$= \sum_{\mathbf{s}} \mathcal{J}_{s_1}(c_1) \cdots \mathcal{J}_{s_N}(c_N) e^{-i\mathbf{d}\cdot\mathbf{s}}, \quad (\text{A7})$$

where  $\mathbf{x} = (x_1, \dots, x_N)$  denotes all possible integer vectors and  $\mathbf{s} = (s_1, \dots, s_N)$  all integer solutions of the Diophantine (i.e., integer) equation

$$\mathbf{z} \cdot \mathbf{s} = z_1 s_1 + \cdots + z_N s_N = n. \quad (\text{A8})$$

A linear Diophantine equation of the form in Eq. (A8) can be solved if and only if the greatest common divisor  $\text{gcd}(z_1, \dots, z_N)$  divides  $n$  [51]. Since the driving force will always contain the fundamental driving frequency, at least one of the elements of  $\mathbf{z}$  equals 1, which implies that Eq. (A8) can be trivially solved for all  $n$ . Without loss of generality we order the elements such that  $z_1 = 1$ . The solution of Eq. (A8) then reads

$$s_1 = n - \sum_{i=2}^N z_i s_i, \quad (\text{A9})$$

where  $s_2, \dots, s_N$  are  $N-1$  integer free parameters that characterize the general solution. Consequently, since  $z_1 = 1$ ,  $N$ -dimensional Bessel functions can be expressed as

$$\mathcal{J}_n^{\mathbf{z}}(\mathbf{c}; \mathbf{d}) = \sum_{s_2, \dots, s_N = -\infty}^{\infty} \mathcal{J}_{s_1}(c_1) \mathcal{J}_{s_2}(c_2) \cdots \mathcal{J}_{s_N}(c_N) e^{-i\mathbf{d}\cdot\mathbf{s}}, \quad (\text{A10})$$

where  $s_1$  is defined in Eq. (A9).

A numerical evaluation of  $N$ -dimensional Bessel functions can be implemented by truncating the infinite sums in Eq. (A10). Specifically, in the numeral implementation of the maximization described in the main text, we examine amplitudes with magnitudes  $|c_i| < 5$ , for which a truncation of  $|s_i|$ ,  $i = 1, \dots, N$ , up to  $\sim 7$  is sufficient. We find that, over a wide range of parameters, this implementation is computationally more efficient than other numerical approaches, such as a Taylor series truncation of the generating function in Eq. (A3). Nonetheless, the dimension of the Bessel function rapidly becomes a limiting factor since the number of terms to evaluate grows with  $N$ . For this reason, it is convenient to work with the lowest dimension possible, which is given by the number of elements in  $\mathbf{z}$  that are different. If a subset  $\mathbf{z}'$  of  $\mathbf{z}$  contains the same elements, i.e.,  $\mathbf{z}' = (z, \dots, z)$ , then the polar parametrization

$$r e^{-i\alpha} \equiv \sum_i c'_i e^{-id'_i} \quad (\text{A11})$$

allows one to express

$$\sum_i c'_i \sin(z\tau - d'_i) = r \sin(z\tau - \alpha), \quad (\text{A12})$$

where  $r$  is real (but not necessarily positive) and  $c'_i, d'_i$  are the elements of  $\mathbf{c}$  and  $\mathbf{d}$  associated with  $\mathbf{z}'$ . In this manner, the dimension of  $\mathbf{z}$  can be reduced by  $\text{dim}(\mathbf{z}') - 1$ . This process can be repeated until all the elements of  $\mathbf{z}$  are different.

## APPENDIX B: ISOTROPIC TUNNELING RATES

In this Appendix we will demonstrate how the driving forces  $\mathbf{F}_{\pm}(t)$  introduced in Eq. (26) lead to isotropic nearest-neighbor (NN) tunneling rates  $g_{\mathbf{a}_k}^0$  and next-nearest-neighbor (NNN) tunneling rates  $\tau_k$  defined after Eqs. (14) and (15), respectively. For this purpose, we shall first find analytical expressions of the Fourier components  $g_{\mathbf{a}_k}^n$  defined after Eq. (20) by means of multidimensional Bessel functions.

We start by considering the force  $\mathbf{F}_+(t)$  in Eq. (26). The quantity  $\chi_{\mathbf{a}_k}(t)$  introduced in Eq. (13) reads

$$\chi_{\mathbf{a}_k}(t) = \sum_{m=1}^N \frac{A_m}{\omega_m} [\sin(\omega_m t - \delta_m) \mathbf{a}_k \cdot \mathbf{e}_1 + \sin(\omega_m t - \delta_m^+) \mathbf{a}_k \cdot \mathbf{e}_2]. \quad (\text{B1})$$

Following the same arguments as in Appendix A, we introduce the polar representation

$$c_m e^{-id_m^k} = \frac{A_m}{\omega_m} (e^{-i\delta_m} \mathbf{a}_k \cdot \mathbf{e}_1 + e^{-i\delta_m^+} \mathbf{a}_k \cdot \mathbf{e}_2) \quad (\text{B2})$$

$$= \frac{A_m}{\omega_m} e^{-i\delta_m} [\mathbf{a}_k \cdot \mathbf{e}_1 - i(-1)^m \mathbf{a}_k \cdot \mathbf{e}_2]. \quad (\text{B3})$$

Importantly, since relative phases  $\delta_m^{(\pm)}$  in Eq. (27) have been chosen to satisfy  $\delta_m^+ - \delta_m = (-1)^m \pi/2$ , the quantities  $c_m$  read

$$c_m = \frac{A_m}{\omega_m} |\mathbf{a}_k| \quad (\text{B4})$$

and, therefore, do not depend on the direction specified by the index  $k$  because the amplitude of the vectors  $\mathbf{a}_k$  is independent of  $k$ . Moreover, from Eq. (B3) we find that the directionality-dependent phases  $d_m^k$  can be expressed as

$$d_m^k = \delta_m + (-1)^m \phi_k, \quad (\text{B5})$$

where  $\phi_k$  denotes the angle of the vector  $\mathbf{a}_k$  with respect to  $\mathbf{e}_1$  and they read  $\phi_1 = \pi/6$ ,  $\phi_2 = 5\pi/6$ , and  $\phi_3 = 3\pi/2$  with the convention introduced in Fig. 1.

Using this representation, the number of terms in Eq. (13) is reduced from  $2N$  to  $N$  such that it can be rewritten as

$$\chi_{\mathbf{a}_k}(t) = \sum_{m=1}^N c_m \sin(\omega_m t - d_m^k). \quad (\text{B6})$$

With the isotropic tunneling rates  $j_0$  of the undriven system, the Fourier components  $g_{\mathbf{a}_k}^n$  can be expressed in terms of  $N$ -dimensional Bessel functions as

$$g_{\mathbf{a}_k}^n = j_0 \mathcal{J}_n^{\mathbf{z}}(\mathbf{c}; \mathbf{d}^k), \quad (\text{B7})$$

where  $\mathbf{c} = (c_1, \dots, c_N)$ ,  $\mathbf{d}^k = (d_1^k, \dots, d_N^k)$ , and  $\mathbf{z} = (z_1, \dots, z_N)$  of the Bessel functions, with  $z_m = \omega_m/\omega$ .

The directionality dependence of the Fourier components  $g_{\mathbf{a}_k}^n$  appears only in the exponential  $e^{-i\mathbf{d}^k \cdot \mathbf{s}}$  of the Bessel function [see Eq. (A10)]. In fact, due to Eq. (B5), the only possible directionality dependence originates from  $\mathbf{p}^k \equiv [-\phi_k, \dots, (-1)^N \phi_k]$  through

$$\begin{aligned} e^{-i\mathbf{p}^k \cdot \mathbf{s}} &= \exp \left[ i \left( n - \sum_{m=2}^N z_m s_m \right) \phi_k - i \sum_{n=2}^N (-1)^m \phi_k s_m \right] \\ &= \exp \left[ i \phi_k \left( n - \sum_{m=2}^N [z_m + (-1)^m] s_m \right) \right], \quad (\text{B8}) \end{aligned}$$

with the integer vector

$$\mathbf{s} = \left( n - \sum_{m=2}^N s_m z_m, s_2, \dots, s_N \right). \quad (\text{B9})$$

From Eq. (B8), the isotropy of the NN tunneling rates  $g_{\mathbf{a}_k}^0$  directly follows. For  $n = 0$ , Eq. (B8) reduces to

$$e^{-i\mathbf{p}^k \cdot \mathbf{s}} = \exp \left( -i3\phi_k \sum_{m=2}^N \frac{[z_m + (-1)^m]}{3} s_m \right). \quad (\text{B10})$$

Because of our choice of  $\omega_m$  in Eq. (28), the quantity  $[z_m + (-1)^m]$  appearing in Eq. (B8) is always a multiple of 3 and, thus,  $[z_m + (-1)^m]/3$  is an integer number. Consequently, since the phases  $\phi_k$  satisfy

$$e^{-i3\phi_1 q} = e^{-i3\phi_2 q} = e^{-i3\phi_3 q} \quad (\text{B11})$$

for arbitrary integers  $q$ , we obtain that  $\mathcal{J}_0(\mathbf{c}; \mathbf{d}^k)$  and hence  $g_{\mathbf{a}_k}^0$  are independent of the direction  $k$ .

Next, we will demonstrate the isotropy of the NNN tunneling rates  $\tau_k$  by showing that

$$\begin{aligned} e^{-i\mathbf{p}^1 \cdot \mathbf{s}} e^{-i\mathbf{p}^2 \cdot \mathbf{s}'} &= e^{-i\mathbf{p}^2 \cdot \mathbf{s}} e^{-i\mathbf{p}^3 \cdot \mathbf{s}'} \\ &= e^{-i\mathbf{p}^3 \cdot \mathbf{s}} e^{-i\mathbf{p}^1 \cdot \mathbf{s}'}, \end{aligned} \quad (\text{B12})$$

with the integer vectors  $\mathbf{s}$  in Eq. (B9) and

$$\mathbf{s}' = \left( -n - \sum_{m=2}^N s'_m z_m, s'_2, \dots, s'_N \right), \quad (\text{B13})$$

which implies

$$\begin{aligned} \mathcal{J}_n^z(\mathbf{c}; \mathbf{d}^1) \mathcal{J}_{-n}^z(\mathbf{c}; \mathbf{d}^2) &= \mathcal{J}_n^z(\mathbf{c}; \mathbf{d}^2) \mathcal{J}_{-n}^z(\mathbf{c}; \mathbf{d}^3) \\ &= \mathcal{J}_n(\mathbf{c}; \mathbf{d}^3) \mathcal{J}_{-n}(\mathbf{c}; \mathbf{d}^1), \end{aligned} \quad (\text{B14})$$

and hence  $\tau_1 = \tau_2 = \tau_3$ .

The quantities  $e^{-i\mathbf{p}^i \cdot \mathbf{s}} e^{-i\mathbf{p}^j \cdot \mathbf{s}'}$  in Eq. (B12) can be obtained with Eq. (B8) and read

$$\begin{aligned} e^{-i\mathbf{p}^i \cdot \mathbf{s}} e^{-i\mathbf{p}^j \cdot \mathbf{s}'} &= \exp \left( -i3\phi_i \sum_{m=2}^N \frac{[z_m + (-1)^m]}{3} s_m \right) \\ &\times \exp \left( -i3\phi_j \sum_{m=2}^N \frac{[z_m + (-1)^m]}{3} s'_m \right) \\ &\times e^{in(\phi_i - \phi_j)}. \end{aligned} \quad (\text{B15})$$

Then, Eq. (B12) directly follows from Eq. (B15) by using Eq. (B11) and the relation  $e^{in(\phi_1 - \phi_2)} = e^{in(\phi_2 - \phi_3)} = e^{in(\phi_3 - \phi_1)}$ , which demonstrates the isotropy of the NNN tunneling rates. The same result can be readily derived for  $\mathbf{F}_-(t)$  by noting that  $\mathbf{F}_-(t)$  is obtained from  $\mathbf{F}_+(t)$  with the substitution  $\omega \rightarrow -\omega$  and  $\delta_n \rightarrow -\delta_n$ .

As a final remark, we would like to mention that the fact that the parametrization of  $z_m$  does not contain multiples of 3 is a result of the  $2\pi/3$  rotational symmetry of the hexagonal lattice, as one can infer from Eqs. (B10), (B11), and (B15).

- 
- [1] C. Nayak, S. Simon, A. Stern, M. Freedman, and S. D. Sarma, *Rev. Mod. Phys.* **80**, 1083 (2008).
- [2] J. Sinova, D. Culcer, Q. Niu, N. A. Sinitsyn, T. Jungwirth, and A. H. MacDonald, *Phys. Rev. Lett.* **92**, 126603 (2004).
- [3] C. L. Kane and E. J. Mele, *Phys. Rev. Lett.* **95**, 226801 (2005).
- [4] C. L. Kane and E. J. Mele, *Phys. Rev. Lett.* **95**, 146802 (2005).
- [5] M. Z. Hasan and C. L. Kane, *Rev. Mod. Phys.* **82**, 3045 (2010).
- [6] D. J. Thouless, M. Kohmoto, M. P. Nightingale, and M. den Nijs, *Phys. Rev. Lett.* **49**, 405 (1982).
- [7] F. D. M. Haldane, *Phys. Rev. Lett.* **61**, 2015 (1988).
- [8] G. Jotzu, M. Messer, R. Desbuquois, M. Lebrat, T. Uehlinger, D. Greif, and T. Esslinger, *Nature* **515**, 237 (2014).
- [9] D. Jaksch and P. Zoller, *New J. Phys.* **5**, 56 (2003).
- [10] A. Eckardt, C. Weiss, and M. Holthaus, *Phys. Rev. Lett.* **95**, 260404 (2005).
- [11] P. Hauke, O. Tieleman, A. Celi, C. Ölschläger, J. Simonet, J. Struck, M. Weinberg, P. Windpassinger, K. Sengstock, M. Lewenstein, and A. Eckardt, *Phys. Rev. Lett.* **109**, 145301 (2012).
- [12] P. Delplace, A. Gómez-León, and G. Platero, *Phys. Rev. B* **88**, 245422 (2013).
- [13] S. K. Baur, M. H. Schleier-Smith, and N. R. Cooper, *Phys. Rev. A* **89**, 051605 (2014).
- [14] M. Bukov, L. D'Alessio, and A. Polkovnikov, *Adv. Phys.* **64**, 139 (2015).
- [15] H. Lignier, C. Sias, D. Ciampini, Y. Singh, A. Zenesini, O. Morsch, and E. Arimondo, *Phys. Rev. Lett.* **99**, 220403 (2007).
- [16] Y.-J. Lin, R. L. Compton, K. Jimenez-Garcia, J. V. Porto, and I. B. Spielman, *Nature (London)* **462**, 628 (2009).
- [17] M. Aidelsburger, M. Atala, S. Nascimbène, S. Trotzky, Y.-A. Chen, and I. Bloch, *Phys. Rev. Lett.* **107**, 255301 (2011).
- [18] J. Struck, C. Ölschläger, R. Le Targat, P. Soltan-Panahi, A. Eckardt, M. Lewenstein, P. Windpassinger, and K. Sengstock, *Science* **333**, 996 (2011).
- [19] A. Eckardt, M. Holthaus, H. Lignier, A. Zenesini, D. Ciampini, O. Morsch, and E. Arimondo, *Phys. Rev. A* **79**, 013611 (2009).
- [20] H. Rabitz, R. de Vivie-Riedle, M. Motzkus, and K. Kompa, *Science* **288**, 824 (2000).
- [21] C. P. Koch and M. Shapiro, *Chem. Rev.* **112**, 4928 (2012).
- [22] S. Conolly, D. Nishimura, and A. Macovski, *IEEE Trans. Med. Imaging* **5**, 106 (1986).
- [23] N. Khaneja, T. Reiss, C. Kehlet, T. Schulte-Herbrüggen, and S. J. Glaser, *J. Magn. Reson.* **172**, 296 (2005).
- [24] N. Timoney, V. Elman, S. Glaser, C. Weiss, M. Johanning, W. Neuhauser, and C. Wunderlich, *Phys. Rev. A* **77**, 052334 (2008).
- [25] F. Platzer, F. Mintert, and A. Buchleitner, *Phys. Rev. Lett.* **105**, 020501 (2010).
- [26] M. Keck, M. M. Müller, T. Calarco, and S. Montangero, *Phys. Rev. A* **92**, 033402 (2015).
- [27] P. Doria, T. Calarco, and S. Montangero, *Phys. Rev. Lett.* **106**, 190501 (2011).
- [28] B. Bartels and F. Mintert, *Phys. Rev. A* **88**, 052315 (2013).
- [29] A. Verdeny, Ł. Rudnicki, C. A. Müller, and F. Mintert, *Phys. Rev. Lett.* **113**, 010501 (2014).

- [30] T. Neupert, L. Santos, C. Chamon, and C. Mudry, *Phys. Rev. Lett.* **106**, 236804 (2011).
- [31] G. Floquet, *Ann. École Norm. Super.* **12**, 47 (1883).
- [32] W. Magnus, *Commun. Pure Appl. Math.* **7**, 649 (1954).
- [33] J. H. Shirley, *Phys. Rev.* **138**, B979 (1965).
- [34] S. Rahav, I. Gilary, and S. Fishman, *Phys. Rev. A* **68**, 013820 (2003).
- [35] A. Verdeny, A. Mielke, and F. Mintert, *Phys. Rev. Lett.* **111**, 175301 (2013).
- [36] N. Goldman and J. Dalibard, *Phys. Rev. X* **4**, 031027 (2014).
- [37] D. Jaksch, C. Bruder, J. I. Cirac, C. W. Gardiner, and P. Zoller, *Phys. Rev. Lett.* **81**, 3108 (1998).
- [38] A. Verdeny and F. Mintert, *Phys. Rev. A* **92**, 033407 (2015).
- [39] Defined in terms of the Hamiltonian  $H_H(\mathbf{k}) = h'_0(\mathbf{k})\mathbb{1} + \sum_{i=1}^3 h'_i(\mathbf{k})\sigma_i$  with  $h'_0(\mathbf{k}) = 2j_2 \cos(\phi) \sum_{i=1}^3 \cos(\mathbf{k} \cdot \mathbf{b}_i)$ ,  $h'_{1,2}(\mathbf{k}) = h_{1,2}(\mathbf{k})$  and  $h'_3(\mathbf{k}) = h_3(\mathbf{k}) - h'_0(\mathbf{k})$ .
- [40] D. Sticlet, F. Piéchon, J.-N. Fuchs, P. Kalugin, and P. Simon, *Phys. Rev. B* **85**, 165456 (2012).
- [41] T. Oka and H. Aoki, *Phys. Rev. B* **79**, 081406 (2009).
- [42] T. Kitagawa, T. Oka, A. Brataas, L. Fu, and E. Demler, *Phys. Rev. B* **84**, 235108 (2011).
- [43] A. G. Grushin, A. Gómez-León, and T. Neupert, *Phys. Rev. Lett.* **112**, 156801 (2014).
- [44] In fact, the forces  $\mathbf{F}_\pm(t)$  in Eq. (26) can lead to complex nearest-neighbor tunneling  $j_1$ , but it is possible to perform a local unitary transformation that eliminates the complex phase without affecting the next-nearest-neighbor tunneling rates. In other words, the complex phase of  $j_1$  can be trivially incorporated in the definitions of the creation and annihilation operators.
- [45] N. Regnault and B. A. Bernevig, *Phys. Rev. X* **1**, 021014 (2011).
- [46] S. Kourtis and M. Daghofer, *Phys. Rev. Lett.* **113**, 216404 (2014).
- [47] M. Weinberg, C. Ölschläger, C. Sträter, S. Prella, A. Eckardt, K. Sengstock, and J. Simonet, *Phys. Rev. A* **92**, 043621 (2015).
- [48] J. Struck, C. Ölschläger, M. Weinberg, P. Hauke, J. Simonet, A. Eckardt, M. Lewenstein, K. Sengstock, and P. Windpassinger, *Phys. Rev. Lett.* **108**, 225304 (2012).
- [49] G. Jotzu, M. Messer, F. Görg, D. Greif, R. Desbuquois, and T. Esslinger, *Phys. Rev. Lett.* **115**, 073002 (2015).
- [50] H. J. Korsch, A. Klumpp, and D. Witthaut, *J. Phys. A* **39**, 14947 (2006).
- [51] L. J. Mordell, *Diophantine Equations* (Academic Press, New York, 1969).